# Mid-infrared Hall effect in thin-film metals: Probing the Fermi surface anisotropy in Au and Cu

J. Černe, D.C. Schmadel, M. Grayson, G.S. Jenkins, J.R. Simpson, and H.D. Drew Department of Physics, University of Maryland, College Park, MD 20741, USA.

# Abstract

A sensitive mid-infrared (MIR, 900-1100 cm<sup>-1</sup>, 112-136 meV) photoelastic polarization modulation technique is used to measure simultaneously Faraday rotation and circular dichroism in thin metal films. These two quantities determine the complex AC Hall conductivity. This novel technique is applied to study Au and Cu thin films at temperatures down to 20 K and magnetic fields up to 8 T. The Hall frequency  $\omega_{\rm H}$  is consistent with band theory predictions. We report the first measurement of the MIR Hall scattering rate  $\gamma_{\rm H}$ , which is significantly lower than that derived from Drude analysis of zero magnetic field MIR transmission measurements. This difference is qualitatively explained in terms of the anisotropy of the Fermi surface in Au and Cu.

#### I. INTRODUCTION

The DC Hall effect is a standard tool for the study of the electronic properties of conducting materials. In the high field limit ( $\omega_c \tau >> 1$ , where  $\omega_c$  is the cyclotron frequency and  $\tau$  is the carrier scattering time) it can can be shown that the Hall coefficient  $R_{\rm H}$  ( $R_{\rm H} \propto 1/n$ ) can give the number density n of carriers. In many novel electronic materials, however, because of the combination of large effective masses m ( $\omega_c \propto \frac{1}{m}$ ) and short defect induced carrier scattering times  $\tau$ , it is not possible to achieve the high field limit of the Hall effect. Under these conditions the Hall effect is sensitive to the defect scattering in the sample, which complicates its interpretation. Also, in many of these interesting materials, electron interactions are strong and the Fermi liquid theory conditions that are assumed in transport theory are possibly not met. Nevertheless, the DC Hall effect has provided interesting and important information on these materials. The AC Hall effect offers the possibility of overcoming the limitations of the DC Hall effect while providing additional information on the electronic structure of materials. While DC transport can be shown to be mainly sensitive to the mean free path of the carriers, AC transport is sensitive to the energy scales of the system: the plasma frequency, the cyclotron frequency and the carrier relaxation rates. At sufficiently high frequencies  $\omega$  ( $\omega \tau >> 1$ ) the AC conductivity becomes insensitive to the impurity scattering, thereby giving information about the electronic structure of the "clean" system. It can provide insight into the physics of many systems ranging from conventional Fermi liquid metals to more exotic metals such as high temperature superconductors<sup>3</sup> and magnetic transition metal oxides.<sup>4</sup>

Within Fermi liquid theory and the relaxation time approximation, and assuming cubic symmetry, the conductivity tensor can be expressed as integrals over the Fermi surface (FS).<sup>5</sup>

$$\sigma_{xx} = \frac{e^2}{(2\pi)^3 \hbar} \oint_{FS} dS |\mathbf{v}(k)| \tilde{\tau}(k)$$
 (1.1a)

$$\sigma_{xy} = \frac{e^3 H}{(2\pi)^3 \hbar^2 c} \oint_{FS} dS \ \mathbf{e_z} \cdot \left[ \mathbf{v}(k)\tilde{\tau}(k) \times \frac{d[\mathbf{v}(k)\tilde{\tau}(k)]}{dk} \right]$$
(1.1b)

where  $\mathbf{v}$  is the carrier velocity, k is the carrier momentum,  $\tilde{\tau} = \tau/(1 - i\omega\tau)$  where  $\tau$  is the scattering time at point k on the FS, H is the magnetic field, e is the electron charge,  $\hbar$  is Planck's constant, c is the speed of light, and  $\mathbf{e_z}$  is the unit vector along the z-axis ( $\mathbf{B} \parallel \mathbf{z}$ ). Since  $\sigma_{xy}$  depends on the cross product  $\mathbf{v} \times \mathbf{dv}$ , flat regions of the FS (where  $\mathbf{v} \parallel \mathbf{dv}$ ) do not contribute to  $\sigma_{xy}$  whereas high curvature regions, which can produce large angular differences between  $\mathbf{v}$  and  $\mathbf{dv}$ , will be heavily weighted in the integral in Eq. 1.1b.

In the study of the AC Hall effect the complex Hall angle  $\theta_H$  is a particularly useful quantity.  $\theta_H$  is defined as

$$\tan \theta_{\rm H} = \frac{\sigma_{\rm xy}}{\sigma_{\rm xx}},\tag{1.2}$$

where  $\sigma_{xx}$  and  $\sigma_{xy}$  are the diagonal and off-diagonal components of the complex magnetoconductivity tensor. Note that  $\tan \theta_{\rm H}$  is independent of film thickness d, which is useful since d may not be accurately known. For a simple (Drude) metal,  $\tan \theta_{\rm H}$  reduces to  $\omega_c \tau$  in the DC limit.  $\theta_{\rm H}$  has proven to be especially interesting in high temperature superconductors where the scattering rate associated with  $\theta_{\rm H}$  shows striking qualitative and quantitative differences from the rate associated with  $\sigma_{xx}$ . This behavior has been cited as evidence for non-Drude and even non-Fermi liquid physics for high temperature superconductors in the normal state.<sup>6–8</sup> Interesting differences in scattering rates can also be found in more conventional materials such as Au and Cu, as will be explored in this paper.

In general  $\tan \theta_{\rm H}$ , as the ratio of two response functions, is a complicated function which does not have a simple closed form. The simplest generalization of  $\theta_{\rm H}$  to finite frequency is:

$$\tan \theta_{\rm H} = \frac{\omega_{\rm H}}{\gamma_{\rm H} - i\omega} \approx \theta_{\rm H},$$
(1.3)

where  $\omega_{\rm H}$  is the Hall frequency and  $\gamma_{\rm H}$  is the Hall scattering frequency. In this experiment, since  $\omega_{\rm H}$  is small compared to  $\omega$  and  $\gamma_{\rm H}$ , we will use the approximation  $\tan \theta_{\rm H} \approx \theta_{\rm H}$  throughout this paper. Equation 1.3 is valid for a Drude metal in which case,  $\omega_{\rm H} = \omega_{\rm c}$  and  $\gamma_{\rm H} = \gamma_{\rm xx}$ , where  $\omega_{\rm c}$  and  $\gamma_{\rm xx}$  are the conventional cyclotron frequency and isotropic Drude scattering rate, respectively. Equation 1.3 is also valid for Fermi liquids for the case of a k independent scattering time. Furthermore, it is the form obtained in several proposed models of the normal state transport in high temperature superconductors.  $^{6-8}$ 

Though  $\sigma_{xy}$  and  $\theta_H$  tend to be small for metals in the MIR (900-1100 cm<sup>-1</sup>), there are a number of advantages in performing these higher frequency measurements. First, the high frequency allows one to avoid impurity scattering or grain boundary effects which may dominate lower frequency measurements. This is especially important in new materials which often contain many impurities. Thus, the MIR measurements can probe the intrinsic optical properties more directly. Furthermore, the MIR measurements allow one to check the trends observed at lower frequencies. Since  $\theta_H$  obeys a sum rule (see Eq. A1),<sup>10</sup> it is very useful to be able to integrate  $\theta_H$  to higher frequencies to verify whether (and where) the Hall angle sum rule saturates or whether there is more relevant physics at even higher frequencies. Finally, since the high frequency behavior of  $\theta_H$  is constrained by the general requirements of response functions, the asymptotic form for  $\theta_H$  in Eqs. 1.3 and A10 becomes more accurate at higher frequencies.

In this paper, we examine the the MIR Hall effect in Au and Cu thin films. We introduce a sensitive photo-elastic polarization modulation technique in Section II A. Section II B describes the samples. Section III presents MIR magneto-optic transmission measurements from 900 cm<sup>-1</sup> to 1100 cm<sup>-1</sup>. We determine the complex conductivity tensor  $\sigma$  at temperatures down to 20 K and magnetic fields up to 8 T. These results suggest that the Hall frequency  $\omega_{\rm H}$  is in good agreement with band theory while the scattering rate  $\gamma_{\rm xx}$  measured in zero magnetic field transmittance measurements. Section IV A presents a qualitative model that is used to discuss these results. The anisotropy of the FS of Au and Cu can explain the differences between the magneto-optic and zero-field scattering rates. Section IV B compares the results for the MIR measurements with DC results. Appendix A provides theoretical background for the expression of  $\theta_{\rm H}$  that is used to analyze the experimental data.

#### II. EXPERIMENT

# A. Polarimetry Measurements

Since  $\omega_{\rm H} << (\gamma_{\rm H}, \omega)$  and since at high frequencies  ${\rm Re}[\theta_{\rm H}] \propto \omega^{-2}$  and  ${\rm Im}[\theta_{\rm H}] \propto \omega^{-1}$  (see Eq. 1.3), the MIR  $\theta_{\rm H}$  in metals is small, on the order of  $10^{-3}$  Rad. Therefore, a sensitive technique is required for the MIR  $\theta_{\rm H}$  measurements. The MIR data are a direct measurement of the Faraday angle  $\theta_{\rm F}$ , which is the optical analogue of the  $\theta_{\rm H}$ .  $\theta_{\rm F}$  is defined as

$$\theta_{\rm F} = \frac{t_{\rm xy}}{t_{\rm xx}} \tag{2.1}$$

where  $t_{xx}$  and  $t_{xy}$  are the complex transmission amplitudes. In the thin film approximation, the relationship between  $\theta_F$  and  $\theta_H$  is given by:

$$\theta_{\rm F} \approx \tan \theta_{\rm F} = \frac{t_{\rm xy}}{t_{\rm xx}} \approx \frac{\frac{4nZ\sigma_{\rm xy}}{(1+Z\sigma_{\rm xx})^2}}{\frac{4n}{1+Z\sigma_{\rm xy}}} = \left(1 + \frac{1}{Z\sigma_{\rm xx}}\right)\theta_{\rm H} \qquad ; \qquad Z = \frac{Z_0 d}{n+1},$$
 (2.2)

where  $Z_0$  is the impedance of free space, n is the substrate index of refraction, and d is the film thickness. As with  $\theta_{\rm H}$ , the small angle approximation applies to  $\theta_{\rm F}$  in this experiment, so  $\tan \theta_{\rm F} \approx \theta_{\rm F}$ . The experimental data was analyzed using finite thickness film calculations, which deviated from the thin film results by less than 10 %. Furthermore, since the conductances  $(\sigma_{\rm xx}d)$  of Au and Cu films are large,  $\frac{1}{Z\sigma_{\rm xx}} << 1$  so  $\theta_{\rm H} \approx \theta_{\rm F}$ . However, in this paper,  $\sigma_{\rm xx}$  is determined through zero magnetic field transmission measurements, and these corrections (less than 15 %) are included in calculating  $\theta_{\rm H}$  and  $\sigma_{\rm xy}$  from  $\theta_{\rm F}$ .

Figure 1 shows the experimental setup for measuring  $\theta_F$ . A CO<sub>2</sub> laser produces linearly polarized MIR radiation (9-11  $\mu$ m, 1100-900 cm<sup>-1</sup>, 112-136 meV). First, a conventional optical chopper modulates this radiation at  $\omega_0$  (80-150 Hz). In this schematic, the laser polarization  $P_L$  is along  $\hat{x}$ . In the Faraday geometry, the radiation then passes through the sample which is located at the center of an 8 T magneto-optical cryostat. In order to sensitively measure both the real and imaginary parts of  $\theta_F$ , the radiation that is transmitted by the sample is analyzed using a photoelastic modulator (PEM).<sup>11</sup> The PEM periodically retards the phase of one linear polarization component  $E_x\hat{x}$  with respect to the orthogonal component  $E_y\hat{y}$  as follows:

$$PEM(E_x\hat{x} + E_y\hat{y}) = E_x e^{i\Delta(t)}\hat{x} + E_y\hat{y}.$$
(2.3)

 $\Delta(t)$  is the sinusoidal phase modulation of  $E_x\hat{x}$  with respect to  $E_y\hat{y}$ , and is given by:

$$\Delta(t) = \beta \cos(\omega_M t), \tag{2.4}$$

where  $\beta$  is the phase modulation amplitude and  $\omega_M$  is the PEM modulation frequency (50 kHz). Since the sample is axially symmetric along B, the transmittance tensor is diagonal when represented in the circular polarization basis. Therefore, changes in the incident polarization only depend on: (1) the relative difference in the phase of left versus right circularly polarized light due to Re[ $\theta_F$ ], which leads to a rotation (Faraday rotation, FR) in the linearly polarized incident light; and (2) the relative difference in the transmission of left versus right circularly polarized light due to Im[ $\theta_F$ ], which introduces ellipticity (circular dichroism, CD) to the linearly polarized incident light. The optical axis of the PEM

is oriented parallel to that of the laser radiation along  $\hat{x}$ , so that no modulation occurs unless the sample produces a  $\hat{y}$ -component in the polarization by either rotating the polarization (FR) or introducing ellipticity to the polarization (CD). Finally, a static linear polarizer  $P_a$  selects the component of the radiation at 45° to  $\hat{x}$ . A liquid nitrogen-cooled mercury-cadmium-telluride (MCT) element detects the radiation, and three lock-in amplifiers demodulate the resulting time-dependent signal. Combining a bright source such as a CO<sub>2</sub> laser with a sensitive MCT detector provides a signal to detector noise level of up to  $10^5$ . The high sensitivity is especially important due to the low transmittance (< 3 %) of the samples used in this experiment. The signal intensity was kept within the linear response regime of the MCT detector.

The FR (Re[ $\theta_F$ ]) and CD (Im[ $\theta_F$ ]) signals are related to the even and odd harmonics of  $\omega_M$ , respectively. These harmonic signals can be normalized by the average signal chopped at  $\omega_0$  to obtain, for small  $\theta_F$ :

$$\frac{I_{2\omega_M}}{I_{\omega_0}} = \frac{4J_2(\beta)\operatorname{Re}[\theta_{\mathrm{F}}]}{1 + |\theta_{\mathrm{F}}|^2 - 2\operatorname{Re}[\theta_{\mathrm{F}}]J_0(\beta)}$$
(2.5a)

$$\frac{I_{3\omega_M}}{I_{\omega_0}} = \frac{4J_3(\beta)\text{Im}[\theta_F]}{1 + |\theta_F|^2 - 2\text{Re}[\theta_F]J_0(\beta)},$$
(2.5b)

where  $I_{n\omega_M}$ ,  $J_n(\beta)$ ,  $I_{\omega_0}$  are the intensity of the *n*th harmonic of  $\omega_M$ , the *n*th order Bessel function, and the average intensity chopped at  $\omega_0$ , respectively. Since  $|\theta_F|^2 << 1$  and  $\beta$  is chosen so that  $J_0(\beta) = 0$ , the denominators in Eqs. 2.5a and 2.5b are unity. The  $3\omega_M$  harmonic signal was chosen in Eq. 2.5b over the fundamental frequency in order to avoid background signals (such as electrical pickup and interference modulation) that occur at  $\omega_M$ . With this technique one can simultaneously measure both the real and imaginary parts of  $\theta_F$  with a sensitivity of approximately 1 part in  $10^4$  and  $4 \times 10^3$ , respectively. The difference in sensitivity for the real and imaginary parts of  $\theta_F$  is mainly due to the fact that at a typical PEM retardance  $\beta \approx 2.39$  radian,  $J_2(\beta) \approx 2 \times J_3(\beta)$ . The great stability of the measurement is due in part to using a single detector to measure all the signals simultaneously, so that detector and source drift can be accurately normalized out.

Though all the parameters in Eqs. 2.5a and 2.5b are measured independently, the calibration of the system is verified by removing the sample and rotating a quarter waveplate in front of the optical magnet shown in Fig. 1. The signals as a function of quarter waveplate orientation angle are consistent with predictions from the initial calibration. For more details on this measurement technique, see Ref. 12.

#### B. Samples

The samples consisted of thin Au and Cu films grown on semiconductor substrates using conventional vacuum thermal deposition techniques. The film thicknesses were on the order of 10 nm, corresponding to DC resistances in the range of  $R_{\square} \approx 6-10~\Omega$ . The thickness was chosen to maximize the quality of the film and the magneto-optic signals while maintaining a transmittance of approximately 5 % at 1000 cm<sup>-1</sup>. Substrates consisted of 0.5 mm thick insulating Si ( $\rho \geq 2000~\Omega$ -cm) or GaAs. The DC residual resistance ratio ( $R_{300~K}/R_{10~K}$ ) for the Au and Cu films is 1.6 and 1.3, respectively. The low temperature resistance is dominated

by interface scattering, as will be shown in Section IV A. Since interference (etalon) effects associated with the substrate can have a strong effect on FR and CD measurements, the substrates were either wedged 1 degree to remove multiply reflected beams or coated with a NiCr broadband antireflection coating.<sup>13</sup> An antireflection coating with  $R_{\square} = 157 \Omega$  for Si and  $R_{\square} = 149 \Omega$  for GaAs reduced the etalon interference fringes to less than 5 % of the transmittance signal.

#### III. RESULTS

Figure 2 plots  $\text{Re}[\theta_{\text{F}}]$  and  $\text{Im}[\theta_{\text{F}}]$  (see Eqs. 2.5a and 2.5b) as a function of magnetic field B at room temperature for a Cu sample. The MIR radiation frequency is 949 cm<sup>-1</sup>. The substrate's background contribution to  $\text{Re}[\theta_{\text{F}}]$  has been removed. Though both Si and GaAs substrates produced signicant  $\text{Re}[\theta_{\text{F}}]$  signal ( $\approx 2-3\times 10^{-3}$  Rad, respectively), their contribution to  $\text{Im}[\theta_{\text{F}}]$  was negligible. The signals are linear in B, as expected.

Figure 3 shows the temperature dependence of  $\theta_{\rm H}$  (a) and  $\theta_{\rm H}^{-1}$  (b) at 1079 cm<sup>-1</sup> and 8 T for a Au sample. The solid (empty) circles represent the real (imaginary) part of  $\theta_{\rm H}$  and  $\theta_{\rm H}^{-1}$ . Note that  ${\rm Im}[\theta_{\rm H}]$  is greater than  ${\rm Re}[\theta_{\rm H}]$  by approximately a factor of four, which suggests that the measurement is approaching the high frequency regime where  ${\rm Im}[\theta_{\rm H}] >> {\rm Re}[\theta_{\rm H}]$ . Though both  ${\rm Re}[\theta_{\rm H}]$  and  ${\rm Im}[\theta_{\rm H}]$  show weak temperature dependence in Fig. 3(a), only the  ${\rm Re}[\theta_{\rm H}^{-1}]$  shows temperature dependence in Fig. 3(b). This is consistent with a temperature dependent  $\gamma_{\rm H}$  and temperature independent  $\omega_{\rm H}$  (see Eqs. 1.3 and A10). The solid triangles in Fig. 3(b) show the DC  $\theta_{\rm H}^{-1}$  at low and high temperatures. The DC  $R_{\rm H}$  measurements were made using the Van der Pauw geometry on the same thin film samples that were examined in the MIR. The DC  $\theta_{\rm H}^{-1}$  is seen to agree well with the MIR  ${\rm Re}[\theta_{\rm H}^{-1}]$ .

Figure 4 shows the frequency dependence of  $\theta_{\rm H}^{-1}$  at 290 K and 8 T.  ${\rm Im}[\theta_{\rm H}^{-1}]$  is represented by empty circles which show a linear increase with frequency, suggesting a frequency independent  $\omega_{\rm H}$  at these frequencies (see Eq. A10). The  ${\rm Im}[\theta_{\rm H}^{-1}]$  data are fitted with a line intersecting the origin, whose slope agrees with band predictions to within 2 %. The  ${\rm Re}[\theta_{\rm H}^{-1}]$  is represented by solid circles and shows no frequency dependence. The DC  $\theta_{\rm H}^{-1}$  is also seen to agree well with the MIR values.

Figure 5 shows the temperature dependence of the Hall frequency  $\omega_{\rm H}$  and Hall scattering rate  $\gamma_{\rm H}$  at 8 T.  $\omega_{\rm H}$  shows no temperature dependence in Fig. 5(a) and agrees well with the value obtained using band theory (solid line). Figure 5(b) shows the MIR  $\gamma_{\rm H}$  at 8 T (solid circles), the MIR  $\gamma_{\rm xx}$  (empty squares), and the DC  $\gamma_{\rm xx}$  (empty triangles). The MIR  $\gamma_{\rm xx}$  is obtained from zero-field transmittance spectra (1000-7000 cm<sup>-1</sup>). These spectra are measured using a Fourier transform spectrometer and are fitted with simple Drude theory to obtain the MIR  $\sigma_{\rm xx}$  and  $\gamma_{\rm xx}$ , which is used to transform  $\theta_{\rm F}$  into  $\theta_{\rm H}$ . The DC  $\gamma_{\rm xx}$  are measured using conventional four probe electrical techniques. Note that  $\gamma_{\rm H}$  is consistently smaller than the MIR  $\gamma_{\rm xx}$  for the Au and Cu samples. The MIR values for  $\gamma_{\rm xx}$  are consistently higher than those obtained using DC measurements, especially at lower temperatures. Though exhibiting a similar temperature dependence, the  $\gamma_{\rm H}$  are significantly lower than both the MIR and DC  $\gamma_{\rm xx}$ . Note that the scattering rates only decrease by 15-30 % at low temperature, which suggests that the scattering rate is dominated by the interfaces of the films (as is discussed in Section IV A).

Table I shows the Hall scattering rates  $\gamma_{\rm H}$  and  $\gamma_{\rm xy}$  along with the zero field scattering rate  $\gamma_{\rm xx}$ . Au films show a greater difference between  $\gamma_{\rm xy}$  and  $\gamma_{\rm xx}$  than the Cu film, with  $\gamma_{\rm xy}/\gamma_{\rm xx} \approx 0.77$  for the former and 0.86 for the latter.

Table II shows the measured and predicted values for the Hall frequency.  $\omega_{\rm H}$  agrees well with predictions from band calculations. For Cu, the measured  $\omega_{\rm H}$  is higher than, but within 10 % of the predicted Hall frequency  $\omega_{\rm H}^{\rm band}$ . For Au the agreement is even better, with a variation of less than 5 %. The linear fit in Fig. 4(a) produces a measured  $\omega_{\rm H}$  that is within 2 % of the band calculated value for Au.

Table III shows the Hall coefficient  $R_{\rm H} = \sigma_{\rm xy}/\sigma_{\rm xx}^2$ , from this and other experiments.  $R_{\rm H}^{\rm band}$  is derived from band calculations while  $R_{\rm H}^{\rm free}$  assumes a spherical FS and reduces to the well-known formula for free electrons  $R_{\rm H}^{\rm free} = -1/nec$ , where n is the electron density and c is the speed of light.  $R_{\rm H}^{\rm bulk}$  are from room temperature DC measurements on bulk samples. Note that the MIR values for  ${\rm Re}[R_{\rm H}]$  agree well with  $R_{\rm H}^{\rm band}$  for both Au and Cu. The MIR  ${\rm Im}[R_{\rm H}]$  are approximately a factor of five to eight times smaller than  ${\rm Re}[R_{\rm H}]$  (see Section IV B). The DC  $R_{\rm H}$  for Au agrees well with  $R_{\rm H}^{\rm free}$  while the DC  $R_{\rm H}$  for Cu agrees better with the MIR measured value than  $R_{\rm H}^{\rm free}$ . The MIR and DC measurements in both samples show little temperature dependence.

#### IV. DISCUSSION

# A. Anisotropic Fermi Surface Model

The difference between  $\gamma_{\rm H}$  and  $\gamma_{\rm xx}$  is a consequence of anisotropic scattering on the FS. This is seen more clearly from Eqs. A4a and A4b for  $\gamma_{\rm xx}$  and  $\gamma_{\rm xy}$ . These quantities correspond to two different averages of the scattering over the FS. From Eq. A4b it is seen that  $\gamma_{\rm xy}$  weights more heavily the regions of the FS with strong curvature.

A simple argument based on the FS anisotropy of Au and Cu can account for the difference between  $\gamma_{xy}$  and  $\gamma_{xx}$ . The anisotropy of the FS in Au and Cu is well-characterized. The high curvature regions near the L point of the FS are referred to as necks while the low curvature regions everywhere else are referred to as bellies. High curvature necks have a larger Hall conductivity  $\sigma_{xy}$  (see Eq. 1.1b) while the lower curvature bellies, which make up a greater fraction of the FS, tend to dominate the longitudinal conductivity  $\sigma_{xx}$ . Furthermore, the scattering rate of carriers in the necks can be different from those in the bellies, with  $\gamma_{xy}$  ( $\gamma_{xx}$ ) tending to represent the characteristic scattering rate for carriers in the neck (belly). In bulk materials, the anisotropy in the scattering rate is due to the anisotropy of the electron-phonon interaction. However, in thin films the scattering is dominated by the film interfaces and different mechanisms are responsible for the anisotropy. We explore one such mechanism, the anisotropy of the Fermi velocity  $v_F$ , in the rest of this Section.

Since the bulk scattering length  $l_0$  of the Au and Cu films at room temperature is roughly a factor of four greater than the thickness of these films, one expects the scattering length  $l_{\rm f}$  in the films to be dominated by interface scattering. The ratio of the film conductivity  $\sigma_{\rm f}$  and bulk conductivity  $\sigma_{\rm 0}$  is given by:<sup>19</sup>

$$\frac{\sigma_{\rm f}}{\sigma_0} \approx \frac{3}{4} \frac{d}{l_0} \ln \left( \frac{l_0}{d} \right) \tag{4.1}$$

where d is the film thickness. The conductivity ratio that is measured in the Au (Cu) film is within 10 % (30 %) of the value predicted by Eq. 4.1, and suggests that the scattering length is dominated by the film thickness rather than impurities or phonons. Since the film consists of randomly oriented grains, and since  $l_{\rm f}$  is independent of k, one expects the average scattering length to be isotropic along the FS and related only to the separation d between film interfaces as implied by Eq. 4.1. For simplicity, we take the scattering time  $\tau$  to be related to the scattering length  $l_{\rm f}$  and Fermi velocity  $v_{\rm F}$  as follows:

$$l = v_{\rm F}\tau \approx d \tag{4.2}$$

The scattering rate  $\gamma$  can then be expressed as:

$$\gamma(k) = \frac{1}{\tau(k)} = \frac{v_{\rm F}(k)}{l_{\rm f}} \tag{4.3}$$

where  $\gamma(k)$  and  $\tau(k)$  are the scattering rate and scattering time of the carriers on the FS. From this simple argument, one can estimate that  $\gamma(\text{neck})$  is related to  $\gamma(\text{belly})$  as follows:

$$\frac{\gamma_{\rm xy}}{\gamma_{\rm xx}} \to \frac{\gamma({\rm neck})}{\gamma({\rm belly})} = \frac{v_{\rm F}({\rm neck})}{v_{\rm F}({\rm belly})} \approx 0.56 \text{ to } 0.65$$
 (4.4)

where the values for  $v_{\rm F}({\rm neck})$  and  $v_{\rm F}({\rm belly})$  represent the typical extrema of  $v_{\rm F}$  at the necks and bellies reported in Refs. 17 and 18. Since the Hall measurements involve contributions from both neck and belly regions, the anisotropy observed in the experiment should be smaller than that predicted by Eq. 4.4, which only involves extremal values of  $v_{\rm F}$ . This can be seen in Table I. In fact, the results in Eq. 4.4 represent an upper limit of the anisotropy. For a more quantitative theoretical comparison, the FS integrals in Eqs. A4a and A4b need to be calculated.

#### B. Comparison of MIR and DC results

The frequency dependence of the values measured in this experiment provides important information about anisotropy and inelastic scattering. In this Section, we will discuss the frequency dependence of  $R_{\rm H}$ ,  $\theta_{\rm H}^{-1}$  and  $\gamma_{\rm xx}$ . The Hall coefficient  $R_{\rm H}$  is shown in Table III. For Au, the MIR value of Re[ $R_{\rm H}$ ] is independent of frequency and temperature and 20 % lower than the DC value. Similar results are found for Cu, but with the low temperature MIR  $R_{\rm H}$  only 10 % smaller than the DC value. This difference between the DC and MIR values for  $R_{\rm H}$  implies anisotropic scattering on the FS (see Appendix A). The MIR values of  $R_{\rm H}$  for Au and Cu are in good agreement with band calculations. On the other hand the DC value for Au for these films (in contrast to the DC  $R_{\rm H}^{\rm bulk}$ ) gives the correct carrier density, presumably fortuitously. The MIR Im[ $R_{\rm H}$ ] is non-zero for both Au and Cu, with a magnitude of 20 % and 12 % of the  $R_{\rm H}$ , respectively. Non-zero Im[ $R_{\rm H}$ ] occurs only for a frequency dependent Re[ $R_{\rm H}$ ], and the magnitude of Im[ $R_{\rm H}$ ] is related to the difference between the DC and MIR Re[ $R_{\rm H}$ ]. Therefore, the larger Im[ $R_{\rm H}$ ] in Au is consistent with the stronger frequency dependence of Re[ $R_{\rm H}$ ] in Au when compared to Cu. The sign of Im[ $R_{\rm H}$ ] is consistent with the relative magnitudes of  $\gamma_{\rm xy}$  and  $\gamma_{\rm xx}$  (see Eqs. A11 and A12b), as found

from a comparison of  $\sigma_{xx}$  with  $\theta_H$ . Indeed,  $\gamma_{xx} \neq \gamma_{xy}$  is due to anisotropic scattering and gives the most revealing information about the anistropy of the scattering.

In the case of the inverse Hall angle the DC value  $\theta_{\rm H}^{-1}$  is in good agreement with Re[ $\theta_{\rm H}^{-1}$ ] in the MIR. However, this is also fortuitous since the asymptotic expression Eq. A10 is not valid at low frequency because of the anisotropy of the scattering on the FS. Moreover, even for isotropic scattering, the AC value of Re[ $\theta_{\rm H}^{-1}$ ] should be larger because of phonon scattering at high frequencies. Therefore it appears that the anisotropy effects and the inelastic scattering effects nearly cancel in this case.

From  $\sigma_{xx}$  we deduce that the DC  $\gamma_{xx}$  is smaller than the IR  $\gamma_{xx}$ . This is expected both from anisotropy of the scattering and its frequency dependence. The effect of anisotropy follows from the general result that  $\langle 1/\tau \rangle \langle \tau \rangle \geq 1$  for averages over the FS, since  $\rho_{DC} \sim \langle \tau \rangle^{-1}$  (Eq 1.1a) and  $\gamma_{xx} \sim \langle \tau^{-1} \rangle$  (Eq A4a). The effect of anisotropic scattering should be comparable to that observed in the Hall coefficient or the difference between  $\gamma_{xx}$  and  $\gamma_{xy}$ . Enhanced electron-phonon scattering in the MIR is also expected due to phonon emission at low temperatures which cannot occur for DC excitation. The phonon emission component to the MIR scattering rate is estimated to be approximately 5 %.<sup>20</sup> The frequency dependence due to anisotropy and electron-phonon interaction is quantitatively consistent with the difference between the MIR and DC  $\gamma_{xx}$ .

#### V. CONCLUSION

We have demonstrated a sensitive MIR photo-elastic polarization modulation technique that can be used to obtain the complex MIR Hall conductivity in thin-film metals. The Hall frequencies obtained from these measurements are consistent with band theory, while the Hall scattering rates are consistently lower than those predicted from Drude analysis of zero magnetic field transmission measurements. This difference can be explained qualitatively in terms of the difference in Fermi velocities, and hence the difference in scattering rates, for carriers in the neck and belly regions of the FS. The neck and belly regions contribute differently to  $\sigma_{xx}$  and  $\sigma_{xy}$ , which can account for the difference in  $\gamma_H$  and  $\gamma_{xx}$ . We hope that further band structure calculations will be made to better quantify these arguments. MIR Hall angle measurements have provided a sensitive probe of the FS anisotropy in thin-film metals, and since a number of theories<sup>6,7</sup> predict an anisotropic FS in high temperature superconductors, this technique may be useful for studying these less conventional materials.

#### ACKNOWLEDGMENTS

This work was supported in part by NSF grant DMR-9705129 and by funding from the NSA.

### APPENDIX A: THEORETICAL BACKGROUND FOR THE AC HALL EFFECT

In this Appendix, we discuss the magneto-conductivity tensor within Fermi Liquid theory $^{21}$  and the reelaxation time approximation. These results provide a useful basis for

analyzing the experimental data. Applying the small angle approximation  $\tan \theta_H \approx \theta_H$ , the sum rule on  $\theta_H$  is  $^{10}$ 

$$\int_0^\infty \text{Re}[\theta_{\rm H}] d\omega = \frac{\pi}{2} \omega_{\rm H}. \tag{A1}$$

Since  $\omega$  is greater than the carrier relaxation rates in the experiment discussed in this paper, it is useful to consider the asymptotic forms of the magneto-optical response functions for large  $\omega \tau$ . For large  $\omega \tau$ 

$$\tilde{\tau}(k) = \frac{1}{\frac{1}{\tau(k)} - i\omega} = \frac{i}{\omega} + \frac{\gamma(k)}{\omega^2} + \cdots,$$
(A2)

where  $\gamma(k) = 1/\tau(k)$  is the k-dependent scattering rate on the FS. The limiting high frequency behavior of the conductivity tensor in Eqs. 1.1a and 1.1b becomes

$$\sigma_{xx} = \sigma_{xx}^{\infty} \left( 1 - i \frac{\gamma_{xx}}{\omega} + \cdots \right) \tag{A3a}$$

$$\sigma_{xy} = \sigma_{xy}^{\infty} \left( 1 - 2i \frac{\gamma_{xy}}{\omega} + \cdots \right). \tag{A3b}$$

 $\gamma_{xx}$  and  $\gamma_{xy}$  are different averages of the scattering over the FS given by:

$$\gamma_{xx} = \frac{\oint_{FS} dS |\mathbf{v}(k)| \gamma(k)}{\oint_{FS} dS |\mathbf{v}(k)|}$$
(A4a)

$$\gamma_{xy} = \frac{\oint_{FS} dS \ \gamma(k) \mathbf{e_z} \cdot \left[ \mathbf{v}(k) \times \frac{d \ \mathbf{v}(k)}{dk} \right]}{\oint_{FS} dS \ \mathbf{e_z} \cdot \left[ \mathbf{v}(k) \times \frac{d \ \mathbf{v}(k)}{dk} \right]}.$$
(A4b)

 $\sigma_{xx}^{\infty}$  and  $\sigma_{xy}^{\infty}$  are given by:

$$\sigma_{\rm xx}^{\infty} = \frac{i\omega_p^2}{4\pi\omega} \tag{A5a}$$

$$\sigma_{\rm xy}^{\infty} = -\frac{\omega_p^2 \omega_{\rm H}}{4\pi\omega^2},\tag{A5b}$$

where  $\omega_p$  and  $\omega_H$  are the plasma frequency and the Hall frequency, respectively, given by integrals over the FS defined below where we have assumed cubic symmetry and used the weak field approximation.

$$\omega_p^2 = \frac{e^2}{2\pi^2 \hbar} \oint_{\text{FS}} dS |\mathbf{v}| \tag{A6}$$

$$\omega_{\rm H} = \frac{eH}{\hbar c} \frac{\oint_{\rm FS} dS \ \mathbf{e_z} \cdot \left[ \mathbf{v} \times \frac{d\mathbf{v}}{dk} \right]}{\oint_{\rm FS} dS \ |\mathbf{v}|} \tag{A7}$$

Consequently, the asymptotic forms of  $\theta_{\rm H}$  and the Hall coefficient  $R_{\rm H}$  are

$$\theta_{\rm H}^{\infty} = \frac{i\omega_{\rm H}}{\omega} \tag{A8}$$

$$R_{\rm H}^{\infty} = \frac{4\pi\omega_{\rm H}}{\omega_p^2} \tag{A9}$$

Keeping the first order terms in  $\tilde{\tau}$  in Eqs. A3a and A3b, one obtains the asymptotic expansions for the inverse Hall angle  $\theta_{\rm H}^{-1}$  and Hall coefficient  $R_{\rm H}$ 

$$\theta_{\rm H}^{-1} = \frac{-i\omega}{\omega_{\rm H}} + \frac{\gamma_{\rm H}}{\omega_{\rm H}} + O\left(\frac{i}{\omega}\right) + O\left(\frac{1}{\omega^2}\right) + \cdots \tag{A10}$$

$$R_{\rm H} = \frac{\sigma_{\rm xy}}{\sigma_{\rm xx}^2} = \frac{4\pi\omega_{\rm H}}{\omega_p^2 B} \left[ 1 + \frac{i}{\omega} \gamma_R + O\left(\frac{1}{\omega^2}\right) + O\left(\frac{i}{\omega^3}\right) + \cdots \right]$$
 (A11)

where B is the magnetic field and

$$\gamma_{\rm H} \equiv 2\gamma_{\rm xy} - \gamma_{\rm xx} \tag{A12a}$$

$$\gamma_R \equiv 2(\gamma_{xx} - \gamma_{xy}). \tag{A12b}$$

Equation A10 for  $\theta_{\rm H}^{-1}$  is particularly useful since the scattering effects and  $\omega_{\rm H}$  can be readily separated. Furthermore, the high frequency asymptotic form is seen to reduce to the simple Drude form of Eq. 1.3. Also, it is seen that  $R_{\rm H}$  becomes frequency dependent only when the scattering rate is not constant on the FS. This follows from either Eq. A11 where the leading frequency dependent term is proportional to  $\gamma_R = 2(\gamma_{\rm xx} - \gamma_{\rm xy})$  (which is zero for isotropic scattering), or in Eqs. 1.1a and 1.1b where a k-independent  $\gamma$  can be taken out of the integrals and exactly cancels in the ratio  $\sigma_{\rm xy}/\sigma_{\rm xx}^2$ .

These expressions can be extended to include frequency-dependent, inelastic scattering in the memory function formalism. <sup>22</sup> In this case  $\gamma(k) - i\omega$  is replaced with  $\Gamma(k,\omega) - i\Sigma(k,\omega) - i\omega = \Gamma(k,\omega) - i\omega(1+\lambda(k,\omega))$ , where  $\Gamma$  and  $\Sigma$  are the real and imaginary parts of the memory function, respectively. In this case simple expressions can be obtained only for k-independent scattering. It is seen that the Hall coefficient is unaffected since the scattering effects cancel. Therefore,  $R_{\rm H}$  remains frequency independent. The result for  $\theta_{\rm H}^{-1}$  is

$$\theta_{\rm H}^{-1} = \frac{\Gamma(\omega) - i\omega(1 + \lambda(\omega))}{\omega_{\rm H}} \tag{A13}$$

Therefore, similar to the behavior of  $\sigma_{xx}$ , the Hall angle has the same form as in the elastic scattering case but with renormalized parameters. The real part of  $\theta_H^{-1}$  gives the scattering function while the imaginary part gives the renormalized Hall frequency  $\omega_H^* = \omega_H/(1+\lambda(\omega))$ . The Hall angle sum rule is satisfied because  $\lambda(\omega) \to 0$  as  $\omega \to \infty$ .

# REFERENCES

- <sup>1</sup> J.M. Harris, Y.F. Yan, and N.P. Ong, Phys. Rev. B **46**, 14293 (1992).
- <sup>2</sup> N.P. Ong, Phys. Rev. B **43**, 193 (1991).
- <sup>3</sup> For example, see S.G. Kaplan, S. Wu, H.-T.S. Lihn, H.D. Drew, Q. Li, D.B. Fenner, J.M. Phillips, and S.Y. Hou, Phys. Rev. Lett. **76**, 696 (1996).
- <sup>4</sup> Y. Tokura et al., J. Phys. Soc. Jpn **63**, 3931 (1994), K. Chabara et al., Appl. Phys. Lett. **63**, 1990 (1993), R. v. Helmholt et al., Phys. Rev. Lett. **71**, 2331 (1993), and S. Jin et al., Science **264**, 413 (1994), S.G. Kaplan, M. Quijada, H.D. Drew, D.B. Tanner, G.C. Xiong, R. Ramesh, C. Kwan, and T. Venkatesan, Phys. Rev. Letters **77**, 2081 (1996).
- <sup>5</sup> The generalization to lower symmetry is given in Refs. 2 and 6.
- <sup>6</sup> A.T. Zheleznyak, V.M. Yakovenko, H.D. Drew, and I.I. Mazin, Phys. Rev. B 57, 3089 (1998).
- <sup>7</sup>L.B. Ioffe and A.J. Millis, Phys. Rev. B **58**, 11631 (1998).
- <sup>8</sup> P.W. Anderson, Phys. Rev. Lett. **67**, 2092 (1991).
- <sup>9</sup> H.D. Drew, S. Wu, and H.-T.S. Lihn, J. Phys.: Condens. Matter **8**, 10037 (1996).
- <sup>10</sup> H.D. Drew and P Coleman, Phys. Rev. Lett. **78**, 1572 (1997).
- <sup>11</sup> Model II/ZS50 from Hinds Instruments, 3175 NW Aloclek Dr., Hillsboro, OR 97124, USA.
- <sup>12</sup> J. Černe, D.C. Schmadel, and H.D. Drew, Instrumentation Paper, in preparation.
- <sup>13</sup> S.W. McKnight, K.P. Stewart, H.D. Drew, and K. Moorjani, Infrared Phys. 27, 327 (1987).
- <sup>14</sup> W.W. Schulz, P.B. Allen, and N. Trivedii, Phys. Rev. B **45**, 10886 (1992).
- <sup>15</sup> D.A. Papaconstantopoulos, *Handbook of the Band Structure of Elemental Solids* (Plenum Press, New York, 1986).
- <sup>16</sup> C. Hurd, The Hall Coefficient of Metals and Alloys (Plenum, New York, 1972).
- <sup>17</sup> B. Lengeler, W.R. Wampler, R.R. Bourassa, K. Mika, K. Wingerath, and W. Uelhoff, Phys. Rev. B 15, 5493 (1977).
- <sup>18</sup> J. Graefenstein, I. Mertig, E. Mrosan, V.N. Antonov, and VL.N. Antonov, Phys. Stat. Sol. (B) **147**, 575 (1988).
- <sup>19</sup> Z.M. Ziman, *Electrons and Phonons* (Oxford University Press, London, 1963).
- $^{20}\,\mathrm{M.A.}$  Biondi and J.A. Rayne, Phys. Rev. **115**, 1522 (1959).
- <sup>21</sup> L.D Landau, Sov. Phys. JETP **3**, 920 (1957); **5**, 101 (1957); and **8**, 70 (1959).
- <sup>22</sup> J. W. Allen and J. C. Mikkelson, Phys. Rev. B **15**, 2952 (1977).

### **FIGURES**

# FIG. 1. A schematic of the experimental setup.

- FIG. 2. The complex Faraday angle  $\theta_{\rm F}$  for a Cu film as a function of magnetic field at 949 cm<sup>-1</sup> and 290 K.
- FIG. 3. The complex Hall angle  $\theta_{\rm H}$  (a) and inverse Hall angle  $\theta_{\rm H}^{-1}$  (b) for Au as a function of temperature at 1079 cm<sup>-1</sup> and 8 T. The solid (empty) circles correspond to the real (imaginary) part of  $\theta_{\rm H}$  and  $\theta_{\rm H}^{-1}$  in the MIR. The solid triangles in (b) show the DC values for  $\theta_{\rm H}^{-1}$ .
- FIG. 4. The complex inverse Hall angle  $\theta_{\rm H}^{-1}$  for Au is shown as a function of frequency at 290 K and 8 T. The solid (empty) circles represent the real (imaginary) part of  $\theta_{\rm H}^{-1}$ . Re[ $\theta_{\rm H}^{-1}$ ] shows no frequency dependence, while the empty circles representing Im[ $\theta_{\rm H}^{-1}$ ] shows a linear temperature dependence as expected in Eq. A10.
- FIG. 5. The Hall frequency  $\omega_{\rm H}$  (a) and Hall scattering rate  $\gamma_{\rm H}$  (b) for Au as a function of temperature at 1079 cm<sup>-1</sup> and 8 T.  $\omega_{\rm H}$  is independent of temperature and agrees well with the prediction from band calculations, which is shown by the solid line in (a). MIR  $\gamma_{\rm H}$  at 8 T (solid circles), the MIR  $\gamma_{\rm xx}$  (empty squares), and the DC  $\gamma_{\rm xx}$  (empty triangles) are shown in (b). Despite large differences in magnitude, these scattering rates show similar temperature dependence.

# **TABLES**

TABLE I. Comparison of the Hall scattering rates  $\gamma_{\rm H}$  and  $\gamma_{\rm xy}$  (see Eq. A12a) obtained from magneto-optic measurements with the longitudinal scattering rate  $\gamma_{\rm xx}$  obtained from a Drude fit to zero magnetic field transmission measurements. Note the strong anisotropy between the  $\gamma_{\rm H}$  and  $\gamma_{\rm xx}$ . All measurements were performed at 290 K.

Sample	Frequency ( $cm^{-1}$ )	$\gamma_{ m H}~({ m cm}^{-1})$	$\gamma_{\rm xy}~({\rm cm}^{-1})$	$\gamma_{\rm xx}~({\rm cm}^{-1})$	$\gamma_{\rm xy}/\gamma_{\rm xx}$
Cu	949	$525\pm55$	$605 \pm 60$	$685 \pm 70$	0.88
Au	1079	$449\pm45$	$585\pm60$	$720\pm76$	0.81

TABLE II. Comparison of the Hall frequency  $\omega_{\rm H}$  with the  $\omega_{\rm H}^{\rm band}$  predicted from band calculations.<sup>14,15</sup> The agreement is within the experimental error. All measurements were performed at 290 K.

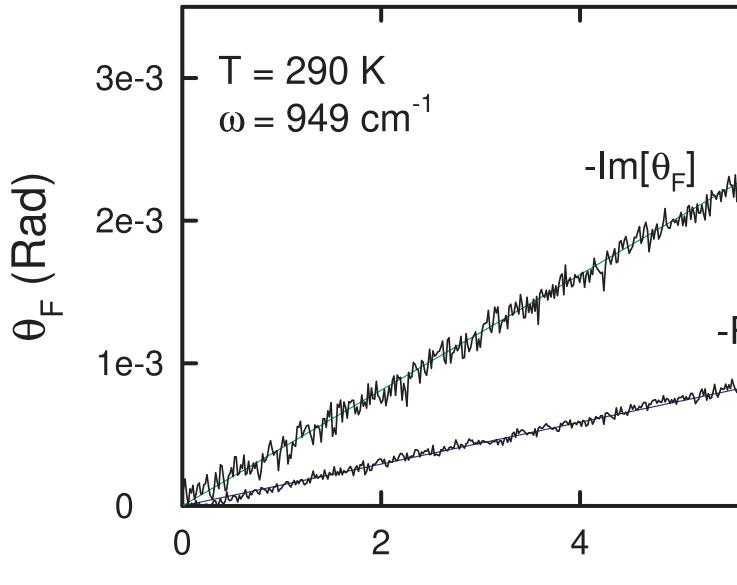
Sample	Frequency ( $cm^{-1}$ )	$\omega_{\mathrm{H}}~(\mathrm{~cm^{-1}})$	$\omega_{\rm H}^{\rm band}~({\rm cm}^{-1})$	$\omega_{ m H}/\omega_{ m H}^{ m band}$
Cu	949	$-4.1 \pm 0.2$	-3.8	1.08
Au	923	$-5.6 \pm 0.3$	-5.5	1.02
Au	1079	$-5.2 \pm 0.3$	-5.5	0.95

TABLE III. Comparison of the MIR and DC Hall coefficients  $R_{\rm H}$ . The units for  $R_{\rm H}$  are  $10^{-11}~{\rm m}^3{\rm C}^{-1}$ . The Cu and Au MIR measurements were performed at 949 cm<sup>-1</sup> and 1079 cm<sup>-1</sup>, respectively.

Sample	T(K)	$MIR R_H$	$DC R_H$	$R_{\rm H}^{ m band}$ Ref. 14	$R_{\rm H}^{\rm free}$ Ref. 14	DC $R_{\rm H}^{\rm bulk}$ Ref. 16
Cu	290	-4.42 -0.465i	-4.28	-5.2	-7.3	-5.17
Cu	40	-4.28 -0.534i	-4.75			
Au	290	-8.04 -1.49i	-9.9	-8.1	-10.5	-7.16
Au	23	-7.96 -1.65i	-10.4			

This figure "fig1.jpg" is available in "jpg" format from:

http://arxiv.org/ps/cond-mat/9907210v1



Magnetic Field (7

